Article

Designing highly efficient oxygen evolution reaction electrocatalyst of high-entropy oxides FeCoNiZrO$_x$: Theory and experiment

The correlations between theoretical potential and d electron density (D_d) of Fe^{3+} ions

Haiqing Zhao, Tao Wang, Can Li, Miaogen Chen, Lengyuan Niu, Yinyan Gong

canli1983@gmail.com

Highlights

The correlator of *d* electron density is adopted for FeCoNiZr-based high entropy oxide

The annealing temperature increases the *d* electron density

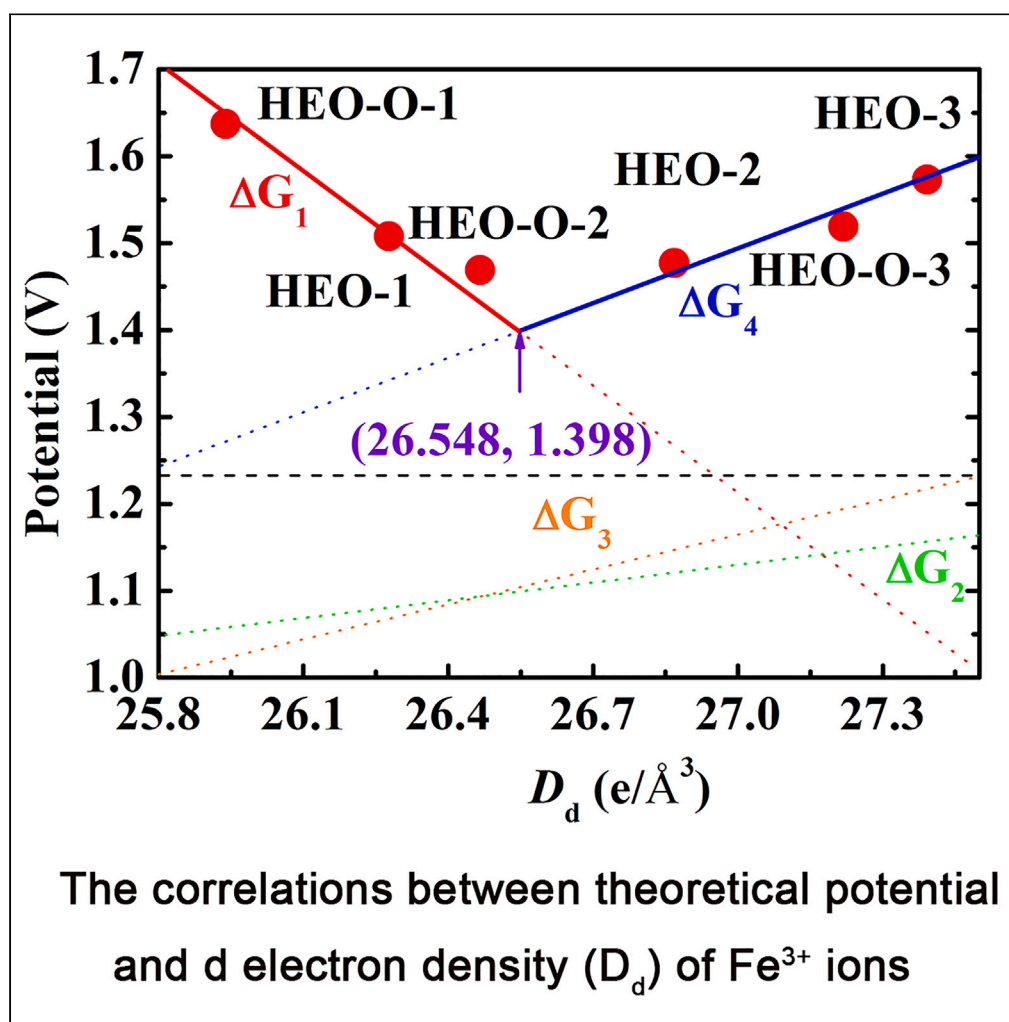FeCoNiZr-based high entropy oxide exhibits low η^{exp} of 245 mV at 10 mA cm^{-2}

Article

Designing highly efficient oxygen evolution reaction electrocatalyst of high-entropy oxides FeCoNiZrOx: Theory and experiment

Haiqing Zhao,[1] Tao Wang,[2] Can Li,[1,4,*] Miaogen Chen,[3] Lengyuan Niu,[1] and Yinyan Gong[1]

SUMMARY

The correlations between the experimental methods and catalytic activities are urgent to be defined for the design of highly efficient catalysts. In this work, a new oxygen evolution reaction electrocatalyst of high-entropy oxide (HEO) FeCoNiZrOx was designed and analyzed by experimental and theoretical methods. On account of the shortened coordinate bond along with the increased annealing temperature, the atomic/electronic structures of active site were adjusted quantitatively with the aid of the pre-designed correlator of d electron density, which contributed to adjust the catalytic activity of HEO specimens. The prepared HEO specimen exhibited the low overpotentials of 245 mV at 10 mA cm^{-2} and 288 mV at 100 mA cm^{-2} with small Tafel slope of 35.66 mV dec^{-1}, fast charge transfer rate, and stable electrocatalytic activity. This strategy would be adopted to improve the catalytic activity of HEO by adjusting the d electron density of transition metal ions with suitable preparation method.

INTRODUCTION

Splitting water into hydrogen and oxygen gases by an electrocatalyst is regarded as a green and effective method to solve the energy crisis and air pollution problems.[1,2] Due to the slow kinetics of oxygen evolution reaction (OER) with complex four-electron reaction processes, the decomposition rate of water molecule is mainly decided by the anode OER.[3–6] Therefore, it is necessary to develop the highly efficient OER electrocatalysts to improve the water decomposition rate. Generally speaking, noble metal-based oxides (such as RuO$_2$ and IrO$_2$) are recognized as the benchmark OER electrocatalysts on account of their high electrocatalytic activity,[7,8] but they are severely restricted by the high costs. Hence, it is important to develop the highly efficient and noble metal-free OER electrocatalysts to replace the noble metal-based oxides.

On account of the similar extra-nuclear electron structures as noble metals, the transition metal (TM) Fe, Co, and Ni elements were considered as the potential candidates to replace the Ru and Ir elements[9–11] in the past decades. Lots of TM-based materials such as oxide,[12] phosphide,[13] layered double hydroxide,[14] alloy,[15–19] and high-entropy oxide (HEO)[20–23] were developed as the noble metal-free electrocatalysts. Among them, multi-component HEO attracted significant attention thanks to its unique advantages of discretionary component, stable structure, diversified active site, and low OER overpotential.[24–27] For example, the synthesized HEO of CoCeNiFeZnCuO$_x$ by successive cation exchange plus electrochemical oxidation methods displayed a low OER overpotential of 211 mV at current density of 10 mA cm^{-2} with a Tafel slope 21 mV dec^{-1}.[28] Previous research indicated that the electrocatalytic OER activity of HEO was strongly associated with the abundant components and diversified active sites.[29–32] Although the abundant components in HEO contributed to provide more composition schemes to adjust the catalytic activity than traditional binary and ternary TM oxides, the design of suitable modification methods became more complex synchronously.

Designing a highly efficient HEO catalyst required the clear understanding of the relationships between surface atomic/electronic structures and catalytic performances at an atomic level. In recent years, the relationships between the local electronic structures and catalytic performances of active sites were widely investigated by numerous catalytic activity descriptors, such as d band center (ε_d), e$_g$ filling, valence band, etc.[33–39] Although the theoretical descriptors exhibited nice correlations with the catalytic activity of various catalysts, the relationships between them and experimental modification methods were still ambiguous, which impeded the design of optimization schemes for highly efficient catalyst. In order to correlate the theoretical descriptor (such as ε_d) with modification methods, a correlator of d electron density (D_d) of TM ions was designed to correlate the modification methods (amorphization and heteroatom incorporation) and OER catalytic activity of
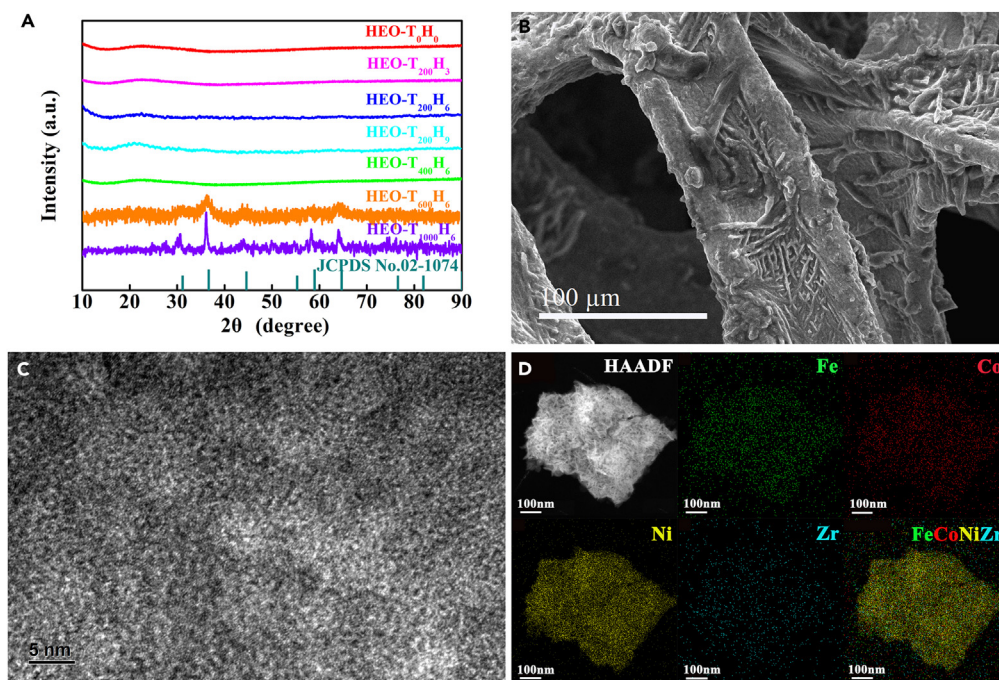
Figure 1. The structural and morphological characterization of specimens
(A) XRD patterns of HEO powder specimens under different annealing temperatures and times.
(B) SEM, (C) TEM, and (D) TEM elemental mapping of HEO-$T_{200}H_6$ specimen.

crystalline FeCo-hydroxyl phosphates and amorphous $(FeCo)_3O_4$ in our previous work.[13,40] To extend the application areas of the correlator, more modification methods and TM-based materials need to be studied for the development of highly efficient catalysts.

In this work, a series of FeCoNiZr-based HEO specimens were prepared via the simple thermostatic water bath plus low-temperature annealing methods. To design the amorphous HEO specimen, the early TM of Zr element plus lately TM of Fe, Co, and Ni elements were selected on account of the different chemical activity and atom size of them. The OER active site and electrocatalytic performances of them were evaluated by experimental measurements and theoretical density functional theory (DFT) simulations. The correlations between annealing temperature and catalytic activity of HEO specimens were analyzed with the aid of the pre-designed correlator. A highly efficient OER electrocatalyst was designed by adjusting the local atomic/electronic structures of active sites with suitable annealing temperature.

RESULTS AND DISCUSSION

Experimental measurements

To confirm the structures of HEO powder specimens, the X-ray diffraction (XRD) patterns of them were measured and compared under different annealing temperatures and times. As shown in Figure 1A, the HEO-T_0H_0 powder specimen exhibited the amorphous phase which was retained under the annealing temperatures of 200°C and 400°C and annealing times of 3, 6, and 9 h. Meanwhile, the phase transition from amorphous to crystalline phase (Co_2NiO_4: Joint Committee on Powder Diffraction Standards (JCPDS) No. 02–1074) appeared under the annealing temperature of 600°C and 1,000°C. Then, all powder specimens were uniformly covered on nickel foam (NF) for scanning electron microscopy (SEM) and high-resolution transmission electron microscopy (HRTEM) measurements. As shown in Figure 1B, the dendritic morphology was observed from the SEM image of HEO-$T_{200}H_6$ specimen which exhibited rougher surface and thus more active sites for catalytic reaction than the other HEO specimens in this work (see Figure S1). Moreover, the micro-structures of HEO-T_0H_0 and HEO-$T_{200}H_6$ specimens were also observed by HRTEM images in Figures 1C and S2; the disordered atomic arrangement also indicated the amorphous structure of HEO specimens. Besides, the TEM elemental mapping images of HEO-$T_{200}H_6$ specimen displayed the uniform distributions of involved Fe, Co, Ni, and Zr elements (see Figure 1D). In order to confirm the composition of HEO specimen, the atomic percentages of all elements were measured by the energy dispersive X-ray spectroscopy (EDS). As shown in Figure S3, the Fe, Co, Ni, Zr, and O elements (C and Au elements originated from carbon pollution and additional spraying) were found in the HEO-$T_{200}H_6$ powder specimen, where the unequal molar ratios of Fe: Co: Ni: Zr (estimated as 3.45: 1.00: 1.45: 2.63) depended on the different precipitation behaviors of various metal cations during co-precipitation. Meanwhile, abundant O element was also measured; it showed that the prepared HEO-$T_{200}H_6$ specimen was regarded as the HEO phase. Finally, according to the aforementioned measurements, the phase structure and surface morphology of the HEO specimens were significantly affected by the annealing temperatures and times.
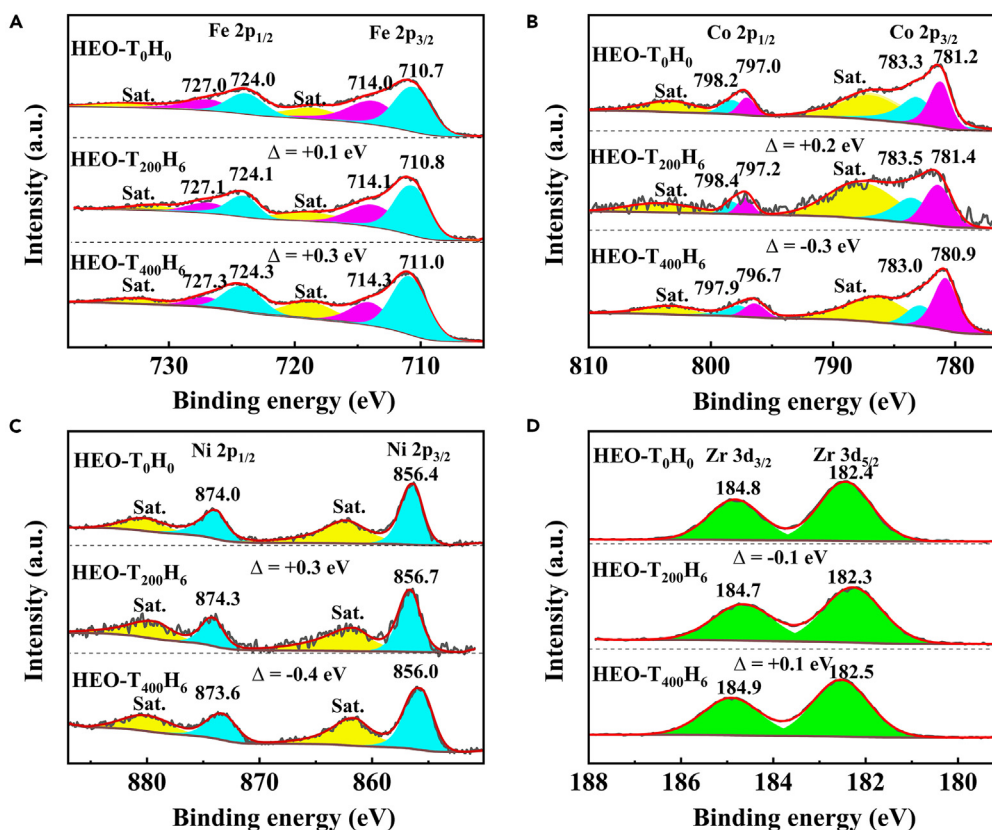
Figure 2. The electronic states of specimens
High-resolution XPS spectra of (A) Fe 2p, (B) Co 2p, (C) Ni 2p, and (D) Zr 3d orbitals in HEO-T_0H_0, HEO-$T_{200}H_6$, and HEO-$T_{400}H_6$ specimens.

The effects of annealing temperature on the TM ion concentrations were also investigated by X-ray photoelectron spectroscopy (XPS) for HEO-T_0H_0, HEO-$T_{200}H_6$, and HEO-$T_{400}H_6$ specimens (see Figures 2 and S4). As shown in the survey spectrum of Figure S4A, the Fe, Co, Ni, Zr, and O elements were observed in three HEO specimens (C element originated from carbon pollution). Meanwhile, the XPS spectra of each element was compared under different annealing temperatures. As shown in Figure 2A, Fe^{2+} and Fe^{3+} ions coexisted in the specimens and the binding energies of Fe 2p orbital were altered by annealing temperature. Comparing to HEO-T_0H_0 specimen, the binding energies of Fe $2p_{1/2}$ and $2p_{3/2}$ orbitals synchronously increased 0.1 and 0.3 eV for HEO-$T_{200}H_6$ and HEO-$T_{400}H_6$ specimens, respectively, which indicated the continuously shortening of Fe-O bond, while the variation trends of binding energies were disordered for Co, Ni, and Zr elements. The binding energies of Co $2p_{1/2}$ and $2p_{3/2}$ (Ni $2p_{1/2}$ and $2p_{3/2}$, O 1s) orbitals synchronously increased 0.2 (0.3, 0.1) eV for HEO-$T_{200}H_6$ specimen and reduced 0.3 (0.4, 0.2) eV for HEO-$T_{400}H_6$ specimen. The binding energies of Zr $3d_{3/2}$ and $3d_{5/2}$ orbitals reduced (increased) 0.1 eV for HEO-$T_{200}H_6$ (HEO-$T_{400}H_6$) specimen. Besides, the binding energies of O 2p orbitals (H_2O, M-OH, and O^{2-}) synchronously increased 0.1 (or reduced 0.2 eV) for HEO-$T_{200}H_6$ (or HEO-$T_{400}H_6$) specimen. The changing trends of O element were consistent with those of Co, Ni, and Zr elements. The different changes of binding energies indicated that the electronic states of TM and O ions could be effectively altered by annealing temperature, which could directly affect the chemical and catalytic activities of active sites.

Besides the changed electronic states, the concentrations of each TM ion were also altered by annealing temperature. As shown in Figure 3A, the percentage of each TM ion was estimated by the normalized integral area of XPS. Meanwhile, the normalized electrochemical active site areas (ECSAs) of all specimens (see Figure 3B) were evaluated based on the measured cyclic voltammetry (CV) curves at 0.81–0.93 V versus reversible hydrogen electrode (see Figure S5), where no faradaic current was produced. Based on the relationships between the percentage of each TM ion and ECSAs of three HEO specimens, as shown in Figure 3C, only the percentage of Fe^{3+} ion exhibited the increasing relationship with the ECSAs values, and Fe^{3+} ion could be the main active site for the HEO specimens, which was consistent with the other FeCoNi-based catalysts.[21,41,42] Moreover, HEO-$T_{200}H_6$ specimen had the largest ECSA (4.33×10^{-3} cm^{-2}) and capacitance (1.06 mF cm^{-2}) compared to HEO-T_0H_0 (ECSA of 3.13×10^{-3} cm^{-2} and capacitance of 0.77 mF cm^{-2}) and HEO-$T_{400}H_6$ (ECSA of 2.82×10^{-3} cm^{-2} and capacitance of 0.71 mF cm^{-2}) specimens. Hence, the percentage of each TM ion and the amount of main active sites were effectively altered by annealing temperature.

The electrocatalytic OER performances of HEO specimens were measured and compared in Figure 4. Based on the electrocatalytic stability test in Figure 4E, the HEO-$T_{200}H_6$ specimen underwent the structural restructuring during the initial 24 h *i-t* test due to the
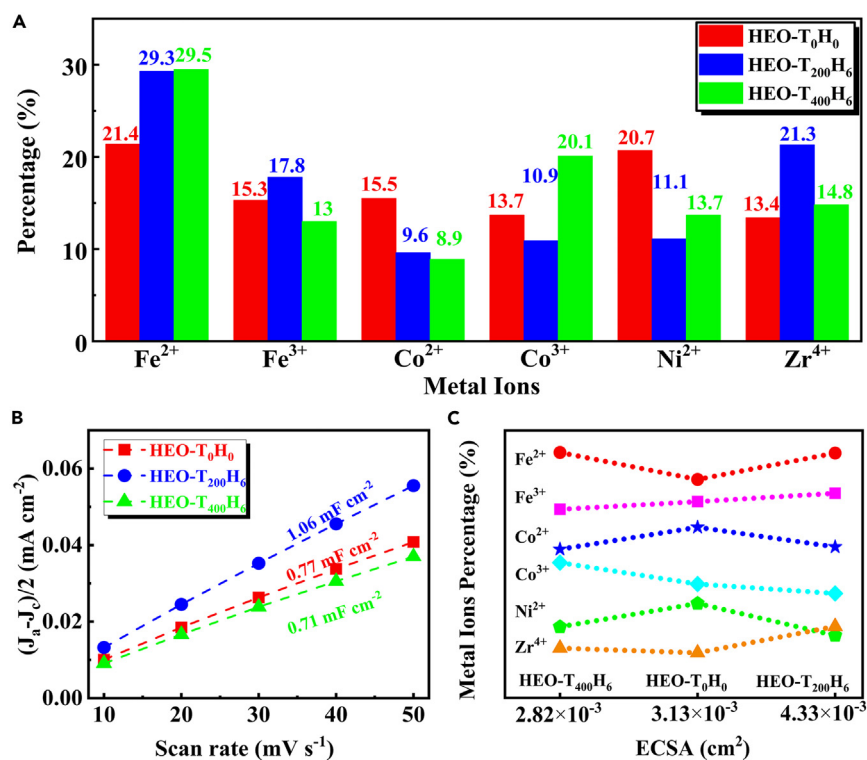
Figure 3. The percentages of metal ions, ECSAs, and the relationship between them

(A) The percentages of metal ions estimated by normalized integral area of XPS.

(B) The capacitive current as a function of scan rate.

(C) The relationship between the percentage of each metal ion and ECSAs of three HEO specimens.

fluctuated current density and then entered into the stable catalytic stage on account of the smooth change of current density at the latter 24 h i-t test, which was also observed from the distinguishing Raman, SEM/TEM images (see Figure S6), and XPS data (Figure S7) before and after 48 h i-t test. Moreover, the OER performances of HEO specimens were remarkably affected by annealing conditions on account of the changed electronic states and the percentage of each TM ion. Thereinto, HEO-$T_{200}H_6$ specimen displayed the lowest experimental OER overpotential (η^{exp}) of 245 mV at 10 mA cm^{-2} and 288 mV at 100 mA cm^{-2} (see Figures 4A and 4B) with the smallest Tafel slope of 35.66 mV dec^{-1} (see Figure 4C), the smallest electrode resistance (see Figure 4D), and the highest turnover frequency (TOF) value (0.091 s^{-1} at the η^{exp} of 350 mV) (see Table S1). The OER performance of HEO-$T_{200}H_6$ specimen was better than that of our pre-designed amorphous $(FeCo)_3O_4$ and FeCo-hydroxyl phosphates (see Figure S8) and comparable with that of the other HEO specimens (see Table S2). Meanwhile, the electrocatalytic stability of HEO-$T_{200}H_6$ specimen was also carried out by long-term electrolysis at a given current density of 10 mA cm^{-2}. As shown in Figure 4E, the HEO-$T_{200}H_6$ specimen maintained 91% current density after 48 h i-t test and the linear sweep voltammetry (LSV) curve stayed in identical tune with the formal curve of HEO-$T_{200}H_6$, which indicated the excellent catalytic stability of HEO-$T_{200}H_6$ specimen.

Theoretical simulations

Since the η^{exp} of HEO specimens were mainly affected by annealing temperature, the enhancement mechanisms of it were analyzed for the HEO specimens. Meanwhile, the variation tendencies of atomic/electronic structures and theoretical OER overpotentials (η^{theory}) were compared with the aid of DFT simulations. On account of the variable TM ion concentrations in HEO specimens under different annealing temperatures (see Figure 3A), the local atomic/electronic structures were also varied, which would necessarily affect the chemical and catalytic activity of activity sites in HEO specimens.

Based on the accepted descriptor of d band center[43–45] (ε_d: estimated by partial density of state (PDOS) of Fe^{3+} ions in Figure S9A) and p band center[46,47] (ε_p: estimated by PDOS of O^{2+} ions around Fe^{3+} ions in Figure S9B), the correlations between ε_d (and ε_p) values and the adsorption free energy of OER intermediates (ΔG_{OH^*}, ΔG_{O^*}, and ΔG_{OOH^*} estimated by Equations 18, 5, 6, and 7 for the stable adsorption structures in Figures S10 and S11) were exhibited in Figures 5A and 5C; the approximate linear relationships between them indicated the excellent descriptive ability of ε_d (and ε_p) for the chemical activity of Fe^{3+} active sites. At the same time, the proportional correlation between ε_d and ε_p values indicated that the chemical activity of Fe^{3+} ion was directly adjusted by its surrounding O^{2-} ions (see
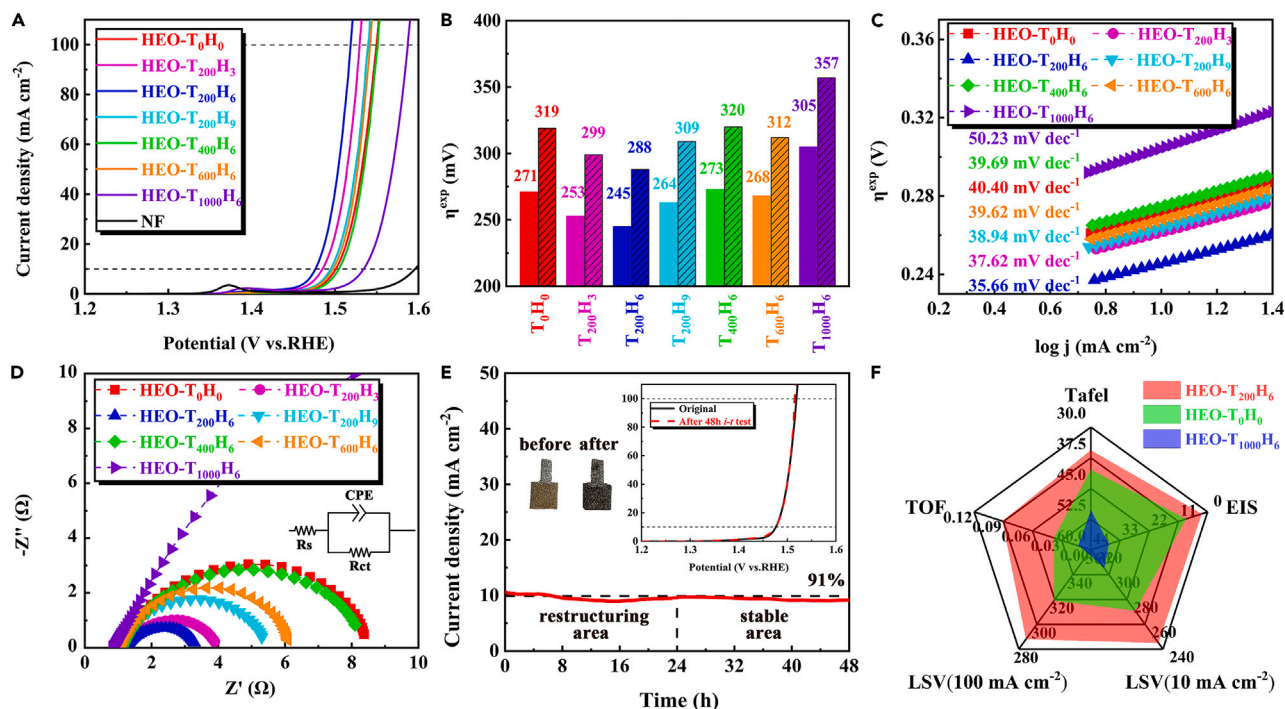
Figure 4. Electrocatalytic OER performance of specimens on NF

(A) The LSV plots of HEO specimens and NF.

(B–D) (B) The η^{exp} at current density of 10 mA cm^{-2} and 100 mA cm^{-2}, (C) Tafel curves, and (D) electrochemical impedance spectroscopy of HEO specimens.

(E) The electrocatalytic stability of HEO-$T_{200}H_6$ during 48 h test.

(F) Radar chart for comparison of comprehensive OER performance of three specimens.

Figure 5B). Moreover, the HEO-O systems exhibited the lower ε_d (and ε_p) energy levels than the corresponding HEO systems (see Table S5), which showed that the covered O group contributed to promote the stability of HEO systems and reduced the chemical activity of Fe^{3+} active sites. Besides the aforementioned changed electronic structures, the magnetism states of HEO and HEO-O systems were also altered on account of the changed spin-up and spin-down orbitals of Fe^{3+} and O^{2-} ions (see Figures S9A and S9B). Based on the estimated average spin density of surface Fe, Co, Ni, and Zr ions (see Table S6 and Figure S9C), the surface Fe ions exhibited the largest average electronic spin moment (μ_B) than the others, and the μ_B value of each TM element was irregularly changed by its coordinated atomic structures (including the covered O group).

In order to correlate the modification method and chemical activity, the pre-designed V_d and correlator D_d were estimated by Equations 19 and 20. On the one hand, the approximate linear relationships between ε_d and D_d values indicated that, as shown in Figure 5B, the local electronic structures of active site (ε_d) could be quantitatively adjusted by its coordination atomic plus electronic structures of D_d.[13,48] On the other hand, the D_d values were increased from HEO-O-1 to HEO-3 systems on account of the shortened Fe-O bond, which were consistent with the experimental XPS measurements. Hence, the pre-designed correlator D_d could effectively correlate the modification method and chemical activity. Moreover, as shown in Figure 5D, the adsorption free energies increased along with the reduced D_d values; the linear relationships between them contributed to ensure the practicality of the correlator D_d for the chemical activity of Fe^{3+} active sites in HEO and HEO-O systems. The self-defined d electron density exhibited the chemical activity of active site which derived from not only the local electronic structures as the d band center but also the coordination atomic structures of active site.

The free energy changes of each one-electron OER step (ΔG_1, ΔG_2, ΔG_3, and ΔG_4 in Figures 6A–6F and Table S4) were further estimated to forecast the η^{theory} of Fe^{3+} active site in each HEO system. As shown in Figure 6A, the first one-electron reaction of $* + OH^- \rightarrow OH^* + e^-$ denoted the OER determining step for HEO-1, HEO-O-1, and HEO-O-2 systems due to its low chemical activity. Compared to HEO-1 (HEO-O-1) system, the Fe-O bonds at active sites were gradually shortened in HEO-2 and HEO-3 (HEO-O-2 and HEO-O-3) systems (see Table S4), which was consistent with the experimental results. The shortened Fe-O bonds increased the D_d values of active sites and reduced the adsorption free energy of each intermediate. On account of the reduced adsorption free energy, the OER determining step transformed the first one-electron reaction to the final one-electron reaction of $OOH^* + OH^- \rightarrow * + O_2(g) + H_2O(l) + e^-$ for HEO-2, HEO-3, and HEO-3-O systems. Meanwhile, the η^{theory} reduced from 407 mV of HEO-O-1 to 239 mV of HEO-O-2 system but increased to 343 mV of HEO-3 system (see Figures 6A–6C). Besides, the chemical and catalytic activities of Fe^{3+} ions were effectively adjusted by the covered O group on HEO-1, HEO-2, and HEO-3 surfaces.
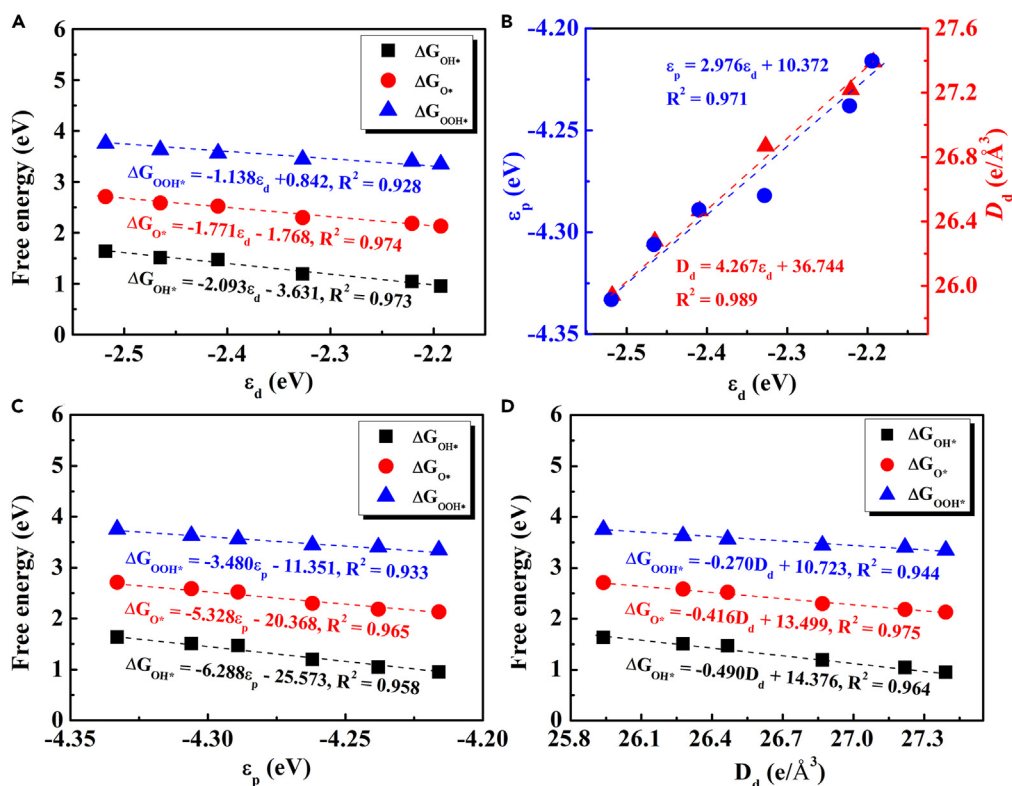
Figure 5. The correlations between the adsorption free energy and local electronic structures

The approximate linear correlations between the adsorption free energy and (A) d band center (ε_d), (D) d electron density (D_d) of Fe^{3+} active sites and (C) p band center (ε_p) of O^{2-} ions in HEO and HEO-O systems.

(B) The approximate linear correlations between ε_d and ε_p (D_d) values.

The correlations between the η^{theory} values and atomic/electronic structures of Fe^{3+} active sites (ε_d, ε_p and D_d) were exhibited in Figures 6D–6I. The "volcanic" correlations between them indicated that the catalytic activity of Fe^{3+} active sites could be directly adjusted by the local atomic/electronic structures. The correlations between the free energy changes of each one-electron OER step and the atomic/electronic structures of Fe^{3+} active sites (ε_d, ε_p and D_d) were fitted and listed in Table S5. In "volcanic" correlations, the HEO-1, HEO-O-1, and HEO-O-2 systems with weak chemical activity located at the red ΔG_1 ridge and the η^{theory} value were decided by ΔG_1 values. Conversely, the HEO-2, HEO-3, and HEO-O-3 systems with strong chemical activity located at the blue ΔG_4 ridge and the η^{theory} value were decided by ΔG_4 values. At tip-top of "volcanic", the HEO system would have the theoretical minimum η^{theory} value of 168 mV as the ε_d, ε_p, and D_d achieved the optimal values of 2.384 eV, 4.284 eV, and 26.548 e/$Å^3$, respectively. Hence, the suitable annealing temperature would be chosen to adjust the atomic and electronic structures of active sites for enhancing the catalytic activity of HEO. This strategy would be adopted to design more highly efficient HEO-based catalysts.

Conclusion

In summary, a new HEO-based electrocatalyst of $(FeCoNiZr)O_x$ was designed and analyzed by experimental and theoretical methods. On account of the shortened coordinate bond and increased d electron density at active sites along with the increased annealing temperature, the atomic/electronic structures of active sites were adjusted with the aid of our pre-designed correlator of D_d, which could quantitatively adjust the electrocatalytic OER activity of the HEO specimens. The prepared HEO-$T_{200}H_6$ specimen exhibited the low η^{exp} of 245 mV at 10 mA cm^{-2} and 288 mV at 100 mA cm^{-2}, the small Tafel slope of 35.66 mV dec^{-1}, fast charge transfer rate, high intrinsic activity (TOF = 0.091 s^{-1} at η^{exp} of 350 mV), and stable electrocatalytic activity. This strategy would be adopted to improve the catalytic activity of HEO by adjusting the d electron density of TM ions with suitable annealing method.

Limitations of the study

Based on the comprehensive analyses by experiment and theory methods, the d electron density of activity ion was explained as a key factor for excellent OER activity. However, in order to gain a deeper understanding of d electron density, more catalytic systems need be investigated by improving the expression of d electron density in the near future.
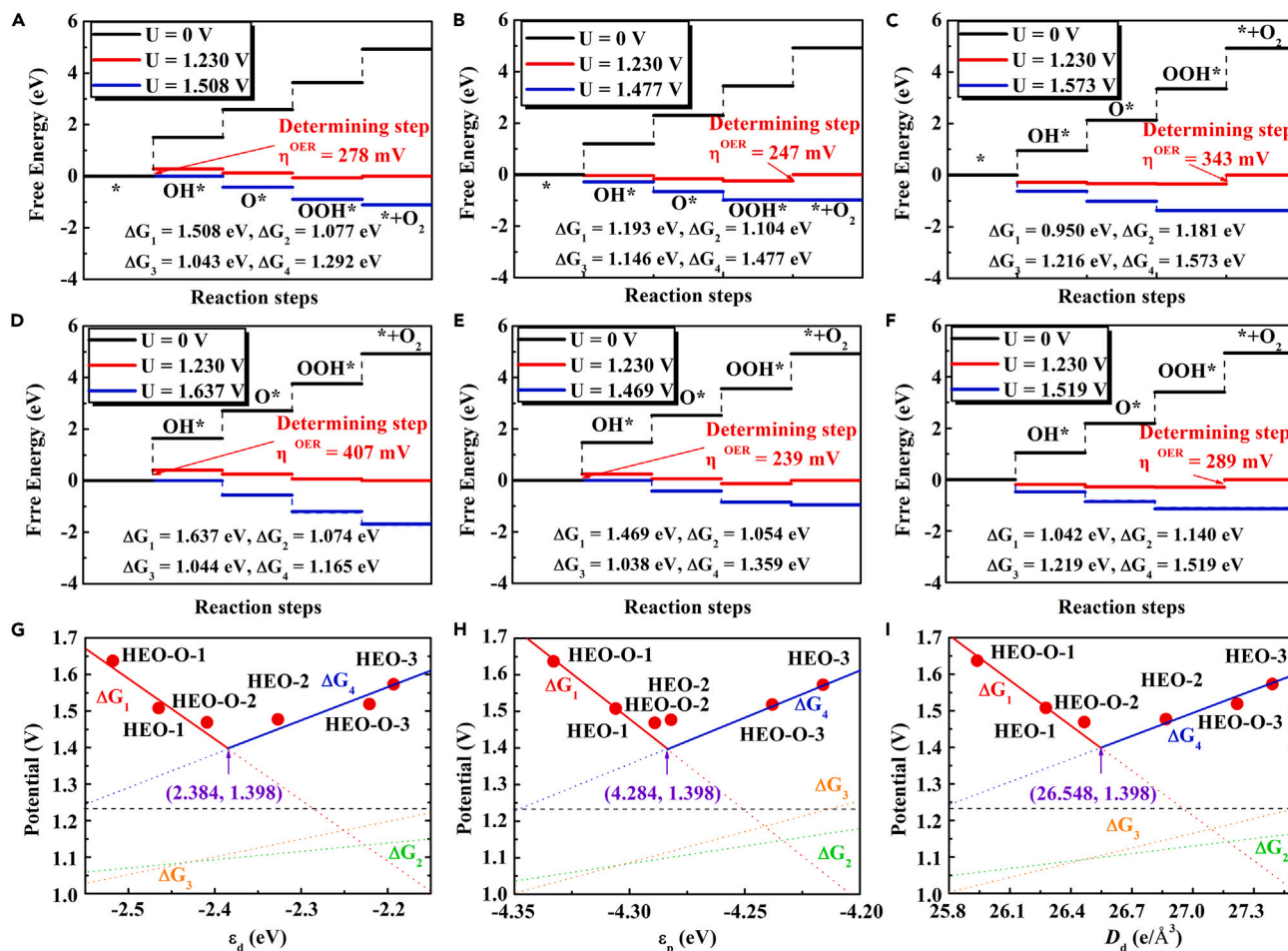
Figure 6. The free energy change curves and the correlations between theoretical potential and local electronic structures
The free energy change curves of (A) HEO-1, (B) HEO-2, (C) HEO-3, (D) HEO-O-1, (E) HEO-O-2, and (F) HEO-O-3 systems during OER. The correlations between theoretical potential and (G) d band center (ε_d), (I) d electron density (D_d) of Fe^{3+} ions, and (H) p band center (ε_p) of O^{2-} ions.

STAR★METHODS

Detailed methods are provided in the online version of this paper and include the following:

- KEY RESOURCES TABLE
- RESOURCE AVAILABILITY
  - Lead contact
  - Materials availability
  - Data and code availability
- METHOD DETAILS
  - Electrochemical measurements
  - Characterizations
  - Computational methods
  - Structural models
  - OER processes

SUPPLEMENTAL INFORMATION

Supplemental information can be found online at https://doi.org/10.1016/j.isci.2023.108718.

AUTHOR CONTRIBUTIONS

H.Z. synthesized and characterized materials, tested the electrochemical performance, performed analysis, prepared figures and schemes, wrote the first and last drafts of the article, and revised submission. C.L. performed DFT analysis and discussions. M.C., L.N., and Y.G. helped in XRD and XPS analysis and revised the first and last drafts of the article. T.W. revised the final draft of the manuscript. C.L. proposed the concept, guided the team, helped in data interpretation, and revised the first and last drafts of the manuscript.

DECLARATION OF INTERESTS

The authors declare no competing interests.

REFERENCES

1. Zhu, L., Li, C., Li, H., Li, H., Wu, Z., Huang, Y., Zhu, X., and Sun, Y. (2022). Adjustable antiperovskite cobalt-based nitrides as efficient electrocatalysts for overall water splitting. J. Mater. Chem. A 10, 15520–15527.

2. Wang, Y., Tao, S., Lin, H., Wang, G., Zhao, K., Cai, R., Tao, K., Zhang, C., Sun, M., Hu, J., et al. (2021). Atomically targeting NiFe LDH to create multivacancies for OER catalysis with a small organic anchor. Nano Energy 81, 105606.

3. Ma, M., Sun, W., Wang, Y., Wang, J., Ma, L., and Yang, Q. (2022). Low-temperature liquid reflux synthesis of core@shell structured Ni@Fe-doped NiCo nanoparticles decorated on carbon nanotubes as a bifunctional electrocatalyst for Zn-air batteries. J. Mater. Chem. A 10, 13088–13096.

4. Park, K.R., Jeon, J., Choi, H., Lee, J., Lim, D.H., Oh, N., Han, H., Ahn, C., Kim, B., and Mhin, S. (2022). NiFe layered double hydroxide electrocatalysts for an efficient oxygen evolution reaction. ACS Appl. Energy Mater. 5, 8592–8600.

5. Wang, X., Yu, M., and Feng, X. (2023). Electronic structure regulation of noble metal-free materials toward alkaline oxygen electrocatalysis. eScience 3, 100141.

6. Zhong, H., Zhang, Q., Yu, J., Zhang, X., Wu, C., Ma, Y., An, H., Wang, H., Zhang, J., Wang, X., and Xue, J. (2023). Fundamental understanding of structural reconstruction behaviors in oxygen evolution reaction electrocatalysts. Adv. Energy Mater. 13, 2301391.

7. Huang, W., Peng, C., Tang, J., Diao, F., Nulati Yesibolati, M., Sun, H., Engelbrekt, C., Zhang, J., Xiao, X., and Mølhave, K.S. (2022). Electronic structure modulation with ultrafine Fe₃O₄ nanoparticles on 2D Ni-based metal-organic framework layers for enhanced oxygen evolution reaction. J. Energy Chem. 65, 78–88.

8. Gou, W., Xia, Z., Tan, X., Xue, Q., Ye, F., Dai, S., Zhang, M., Si, R., Zou, Y., Ma, Y., et al. (2022). Highly active and stable amorphous IrOₓ/CeO₂ nanowires for acidic oxygen evolution. Nano Energy 104, 107960.

9. Shrestha, N.K., Patil, S.A., Han, J., Cho, S., Inamdar, A.I., Kim, H., and Im, H. (2022). Chemical etching induced microporous nickel backbones decorated with metallic Fe@hydroxide nanocatalysts: An efficient and sustainable OER anode toward industrial alkaline water-splitting. J. Mater. Chem. A 10, 8989–9000.

10. Bai, J., Wang, J., Liu, P., Huang, J., Shang, X., and Chao, S. (2022). Three-dimensional flower-like Co-based metal organic frameworks as efficient multifunctional catalysts towards oxygen reduction, oxygen evolution and hydrogen evolution reactions. Int. J. Hydrogen Energy 47, 30484–30493.

11. Wan, K., Luo, J., Zhang, X., Subramanian, P., and Fransaer, J. (2020). In-situ formation of Ni (oxy)hydroxide on Ni foam as an efficient electrocatalyst for oxygen evolution reaction. Int. J. Hydrogen Energy 45, 8490–8496.

12. Qian, Y., Xu, X., He, Y., Lei, L., Xia, Y., and Zhang, X. (2022). A novel monoclinic metal oxide catalyst for oxygen evolution reactions in alkaline media. Inorg. Chem. Front. 9, 941–949.

13. Xia, J., Li, C., Gong, Y., Niu, L., Chen, M., and Xu, S. (2022). Designing of highly-efficient oxygen evolution reaction electrocatalyst FeCo-hydroxyl phosphates: Theory and experiment. Chem. Eng. J. 446, 137151.

14. Liu, J., Zhou, J., Liu, S., Chen, G., Wu, W., Li, Y., Jin, P.J., and Xu, C.L. (2020). Amorphous NiFe-layered double hydroxides nanosheets for oxygen evolution reaction. Electrochim. Acta 14, 15205–15213.

15. Sharma, L., Katiyar, N.K., Parui, A., Das, R., Kumar, R., Tiwary, C.S., Singh, A.K., Halder, A., and Biswas, K. (2022). Low-cost high entropy alloy (HEA) for high-efficiency oxygen evolution reaction (OER). Nano Res. 15, 4799–4806.

16. Huang, K., Zhang, B., Wu, J., Zhang, T., Peng, D., Cao, X., Zhang, Z., Li, Z., and Huang, Y. (2020). Exploring the impact of atomic lattice deformation on oxygen evolution reactions based on a sub-5 nm pure face-centred cubic high-entropy alloy electrocatalyst. J. Mater. Chem. A 8, 11938–11947.

17. Lei, Z., Liu, X., Wu, Y., Wang, H., Jiang, S., Wang, S., Hui, X., Wu, Y., Gault, B., Kontis, P., et al. (2018). Enhanced strength and ductility in a high-entropy alloy via ordered oxygen complexes. Nature 563, 546–550.

18. Li, Z., Pradeep, K.G., Deng, Y., Raabe, D., and Tasan, C.C. (2016). Metastable high-entropy dual-phase alloys overcome the strength-ductility trade-off. Nature 534, 227–230.

19. Maulana, A.L., Chen, P.C., Shi, Z., Yang, Y., Lizandara-Pueyo, C., Seeler, F., Abruña, H.D., Muller, D., Schierle-Arndt, K., and Yang, P. (2023). Understanding the structural evolution of IrFeCoNiCu high-entropy alloy nanoparticles under the acidic oxygen evolution reaction. Nano Lett. 23, 6637–6644.

20. Abdelhafiz, A., Wang, B., Harutyunyan, A.R., and Li, J. (2022). Carbothermal shock synthesis of high entropy oxide catalysts: Dynamic structural and chemical reconstruction boosting the catalytic activity and stability toward oxygen evolution reaction. Adv. Energy Mater. 12, 2200742.

21. Nguyen, T.X., Huang, Z.T., and Ting, J.M. (2021). Iron-concentration adjusted multi-metal oxides for optimized oxygen evolution reaction performance. Appl. Surf. Sci. 570, 151160.

22. Jiang, S., Tian, K., Li, X., Duan, C., Wang, D., Wang, Z., Sun, H., Zheng, R., and Liu, Y. (2022). Amorphous high-entropy non-precious metal oxides with surface reconstruction toward highly efficient and durable catalyst for oxygen evolution reaction. J. Colloid Interface Sci. 606, 635–644.

23. Li, M., Song, M., Ni, W., Xiao, Z., Li, Y., Jia, J., Wang, S., and Wang, Y. (2023). Activating surface atoms of high entropy oxides for enhancing oxygen evolution reaction. Chin. Chem. Lett. 34, 107571.

24. He, L., Kang, H., Hou, G., Qiao, X., Jia, X., Qin, W., and Wu, X. (2023). Low-temperature synthesis of nano-porous high entropy spinel oxides with high grain boundary density for oxygen evolution reaction. Chem. Eng. J. 460, 141675.

25. Wang, B., Yao, J., Wang, J., and Chang, A. (2022). Spinel-type high-entropy (Co₀.₂Mn₀.₂Fe₀.₂Zn₀.₂Ti₀.₂)₃O₄ oxides constructed from disordered cations and oxygen vacancies. J. Alloys Compd. 897, 163188.

26. Zhang, Y., Lu, T., Ye, Y., Dai, W., Zhu, Y., and Pan, Y. (2020). Stabilizing oxygen vacancy in entropy-engineered $CoFe_2O_4$-type catalysts for Co-prosperity of efficiency and stability in an oxygen evolution reaction. ACS Appl. Mater. Interfaces *12*, 32548–32555.

27. Li, X., Zhang, Z., Shen, M., Wang, Z., Zheng, R., Sun, H., Liu, Y., Wang, D., and Liu, C. (2022). Highly efficient oxygen evolution reaction enabled by phosphorus-boron facilitating surface reconstruction of amorphous high-entropy materials. J. Colloid Interface Sci. *628*, 242–251.

28. Huang, W., Zhang, J., Liu, D., Xu, W., Wang, Y., Yao, J., Tan, H.T., Dinh, K.N., Wu, C., Kuang, M., et al. (2020). Tuning the electronic structures of multimetal oxide nanoplates to realize favorable adsorption energies of oxygenated intermediates. ACS Nano *14*, 17640–17651.

29. Wang, D., Jiang, S., Duan, C., Mao, J., Dong, Y., Dong, K., Wang, Z., Luo, S., Liu, Y., and Qi, X. (2020). Spinel-structured high entropy oxide $(FeCoNiCrMn)_3O_4$ as anode towards superior lithium storage performance. J. Alloys Compd. *844*, 156158.

30. Wang, D., Duan, C., He, H., Wang, Z., Zheng, R., Sun, H., Liu, Y., and Liu, C. (2023). Microwave solvothermal synthesis of component-tunable high-entropy oxides as high-efficient and stable electrocatalysts for oxygen evolution reaction. J. Colloid Interface Sci. *646*, 89–97.

31. Yang, X., Liping, S., Qiang, L., Lihua, H., and Hui, Z. (2022). Co-prosperity of electrocatalytic activity and stability in high entropy spinel $(Cr_{0.2}Mn_{0.2}Fe_{0.2}Ni_{0.2}Zn_{0.2})_3O_4$ for the oxygen evolution reaction. J. Mater. Chem. A *10*, 17633–17641.

32. Iwase, K., and Honma, I. (2022). High-entropy spinel oxide nanoparticles synthesized via supercritical hydrothermal processing as oxygen evolution electrocatalysts. ACS Appl. Energy Mater. *5*, 9292–9296.

33. Sun, Y., Zhao, Z., Wu, S., Li, W., Wu, B., Liu, G., Chen, G., Xu, B., Kang, B., Li, Y., and Li, C. (2020). Engineering of the d-band center of perovskite cobaltite for enhanced electrocatalytic oxygen evolution. ChemSusChem *13*, 2671–2676.

34. Zhang, R., Wei, Z., Ye, G., Chen, G., Miao, J., Zhou, X., Zhu, X., Cao, X., and Sun, X. (2021). "d-Electron Complementation" Induced V-Co Phosphide for Efficient Overall Water Splitting. Adv. Energy Mater. *11*, 2101758.

35. Song, M., Lu, X., Du, M., Chen, Z., Zhu, C., Xu, H., Cheng, W., Zhuang, W., Li, Z., and Tian, L. (2022). Electronic and architecture engineering of hammer-shaped $Ir-NiMoO_4-ZIF$ for effective oxygen evolution. CrystEngComm *24*, 5995–6000.

36. Bo, X., Zan, L., Jia, R., Dastafkan, K., and Zhao, C. (2022). The nature of synergistic effects in transition metal oxides/in-situ intermediate-hydroxides for enhanced oxygen evolution reaction. Curr. Opin. Electrochem. *34*, 100987.

37. Zhou, C., Chen, X., Liu, S., Han, Y., Meng, H., Jiang, Q., Zhao, S., Wei, F., Sun, J., Tan, T., and Zhang, R. (2022). Superdurable bifunctional oxygen electrocatalyst for high-performance zinc-air batteries. J. Am. Chem. Soc. *144*, 2694–2704.

38. Flores-Lasluisa, J.X., Huerta, F., Cazorla-Amorós, D., and Morallón, E. (2022). Transition metal oxides with perovskite and spinel structures for electrochemical energy production applications. Environ. Res. *214*, 113731.

39. Luo, D., Yang, B., Mei, Z., Kang, Q., Chen, G., Liu, X., and Zhang, N. (2022). Tuning the d-band states of Ni-based serpentine materials via Fe^{3+} doping for efficient oxygen evolution reaction. ACS Appl. Mater. Interfaces *14*, 52857–52867.

40. Tan, Q., Xiao, R., Yao, X., Xiong, T., Li, J., Hu, Y.W., Huang, Y., and Balogun, M.S. (2022). Non-oxygen anion-regulated in situ cobalt based heterojunctions for active alkaline hydrogen evolution catalysis. Chem. Eng. J. *433*, 133514.

41. Bai, L., Wen, X., and Guan, J. (2019). Amorphous Fe-Co-Ni oxide for oxygen evolution reaction. Mater. Today Energy *12*, 311–317.

42. Friebel, D., Louie, M.W., Bajdich, M., Sanwald, K.E., Cai, Y., Wise, A.M., Cheng, M.J., Sokaras, D., Weng, T.C., Alonso-Mori, R., et al. (2015). Identification of highly active Fe sites in (Ni,Fe)OOH for electrocatalytic water splitting. J. Am. Chem. Soc. *137*, 1305–1313.

43. Cai, M., Zhu, Q., Wang, X., Shao, Z., Yao, L., Zeng, H., Wu, X., Chen, J., Huang, K., and Feng, S. (2023). Formation and stabilization of NiOOH by introducing alpha-FeOOH in LDH: Composite electrocatalyst for oxygen evolution and urea oxidation reactions. Adv. Mater. *35*, e2209338.

44. Zhang, L., Jang, H., Liu, H., Kim, M.G., Yang, D., Liu, S., Liu, X., and Cho, J. (2021). Sodium-decorated amorphous/crystalline RuO_2 with rich oxygen vacancies: A robust pH-universal oxygen evolution electrocatalyst. Angew. Chem. Int. Ed. *60*, 18821–18829.

45. Chen, J., Long, Q., Xiao, K., Ouyang, T., Li, N., Ye, S., and Liu, Z.Q. (2021). Vertically-interlaced NiFeP/MXene electrocatalyst with tunable electronic structure for high-efficiency oxygen evolution reaction. Sci. Bull. *66*, 1063–1072.

46. Liu, Y., Sakthivel, T., Hu, F., Tian, Y., Wu, D., Ang, E.H., Liu, H., Guo, S., Peng, S., and Dai, Z. (2023). Enhancing the d/p-band center proximity with amorphous-crystalline interface coupling for boosted pH-robust water electrolysis. Adv. Energy Mater. *13*.

47. Zhou, S., Pei, W., Zhao, Y., Yang, X., Liu, N., and Zhao, J. (2021). Low-dimensional non-metal catalysts: principles for regulating p-orbital-dominated reactivity. npj Comput. Mater. *7*, 186.

48. Shi, Y., Pan, H., Xia, J., Li, C., Gong, Y., Niu, L., Liu, X., Sun, C.Q., and Xu, S. (2021). Designing of highly efficient oxygen evolution reaction electrocatalysts utilizing a correlation factor: Theory and experiment. ACS Appl. Mater. Interfaces *13*, 30533–30541.

49. Segall, M.D., Lindan, P.J.D., Probert, M.J., Pickard, C.J., Hasnip, P.J., Clark, S.J., and Payne, M.C. (2002). First-principles simulation: Ideas, illustrations and the CASTEP code. J. Phys. Condens. Matter *14*, 2717–2744.

50. Hamann, D.R., Schlüter, M., and Chiang, C. (1979). Norm-conserving pseudopotentials. Phys. Rev. Lett. *43*, 1494–1497.

51. Perdew, J.P., Burke, K., and Ernzerhof, M. (1996). Generalized gradient approximation made simple. Phys. Rev. Lett. *77*, 3865–3868.

52. Grimme, S. (2006). Semiempirical GGA-type density functional constructed with a long-range dispersion correction. J. Comput. Chem. *27*, 1787–1799.

53. Anisimov, V.I., Zaanen, J., and Andersen, O.K. (1991). Band theory and mott insulators: Hubbard U instead of stoner I. Phys. Rev. B *44*, 943–954.

54. Li, H., Wu, Y., Li, L., Gong, Y., Niu, L., Liu, X., Wang, T., Sun, C., and Li, C. (2018). Adjustable photocatalytic ability of monolayer $g-C_3N_4$ utilizing single-metal atom: Density functional theory. Appl. Surf. Sci. *457*, 735–744.

55. Sultan, S., Tiwari, J.N., Singh, A.N., Zhumagali, S., Ha, M., Myung, C.W., Thangavel, P., and Kim, K.S. (2019). Single atoms and clusters based nanomaterials for hydrogen evolution, oxygen evolution reactions, and full water splitting. Adv. Energy Mater. *9*, 1900624.

56. Wu, Y., Li, C., Liu, W., Li, H., Gong, Y., Niu, L., Liu, X., Sun, C., and Xu, S. (2019). Unexpected monoatomic catalytic-host synergetic OER/ORR by graphitic carbon nitride: Density functional theory. Nanoscale *11*, 5064–5071.

57. Chen, M., Chang, W., Shi, Y., Liu, W., and Li, C. (2021). Design of highly efficient $g-C_3N_4$-based metal monoatom catalysts by two extra-NM_1 atoms: Density functional theory simulations. Phys. Chem. Chem. Phys. *23*, 11472–11478.

58. Pan, H., Wu, Y., Li, C., Li, H., Gong, Y., Niu, L., Liu, X., Sun, C.Q., and Xu, S. (2020). Efficient bi-directional OER/ORR catalysis of metal-free $C_6H_4NO_2/g-C_3N_4$: Density functional theory approaches. Appl. Surf. Sci. *531*, 147292.

59. Mann, J.B. (1968). Atomic Structure Calculations II. Hartree-Fock Wave Functions and Radial Expectation Values: Hydrogen to Lawrencium. LA-3691 (Los Alamos Scientific Laboratory).

STAR★METHODS

KEY RESOURCES TABLE

REAGENT or RESOURCE	SOURCE	IDENTIFIER
Chemicals, peptides, and recombinant proteins		
$FeSO_4 \cdot 7H_2O$	Aladdin, China	CAS no. 7782-63-0
$CoCl_2 \cdot 6H_2O$	Aladdin, China	CAS no. 7791-13-1
$NiCl_2 \cdot 6H_2O$	Aladdin, China	CAS no. 7791-20-1
$ZrCl_4$	Aladdin, China	CAS no. 10026-11-6
$C_6H_{12}O_6$	Aladdin, China	CAS no. 50-99-7
$C_2H_6O_2$	Aladdin, China	CAS no. 107-21-1
KOH	Aladdin, China	CAS no. 1310-58-3
NaH_2PO_2	Aladdin, China	CAS no. 7681-53-0
Nafion perfluorinated resin 5% in alcohol	RHAWN, China	CAS no. 31175-20-9
Ni foam	MTI, China	N/A
Software and algorithms		
Origin 8	Origin Lab	N/A
CHI 660E	CHI Instruments	N/A
MS 8.0	Materials Studio	N/A

RESOURCE AVAILABILITY

Lead contact

Further information and requests for resources and reagents should be directed to and will be fulfilled by the lead contact, Can Li (canli1983@gmail.com).

Materials availability

Catalysts are available up on request.

Data and code availability

- Data reported in this article will be shared by the lead contact on request.
- This paper does not report original codes.
- Any additional information required to reanalyze the data reported in this paper is available from the lead contact upon request.

METHOD DETAILS

Firstly, the solution A was prepared by adding a bit of 0.3 mol/L KOH solution into 0.1 mol/L NaH_2PO_2 with pH = 7. The solution B was prepared by dissolving 0.1 mol/L $FeSO_4 \cdot 7H_2O$, $CoCl_2 \cdot 6H_2O$, $NiCl_2 \cdot 6H_2O$ and $ZrCl_4$ into 5 mL deionized water. The solution C was prepared by adding 1 g $C_6H_{12}O_6$ and 5 mL $C_2H_6O_2$ into 20 mL deionized water. Secondly, 15 mL solution A was slowly dripped into solution B for the uniform mixed solution D. Then, 25 mL solution C was dripped into the mixed solution D for the uniform mixed solution E. Thirdly, the mixed solution E was transferred to an electric-heated thermostatic water bath at 85°C for 30 min. The precipitates were collected, washed thoroughly by water and ethanol and then dried at 60°C. Finally, each specimen was obtained by annealing in air under temperatures of 200, 400, 600 and 1000 ºC and times of 3, 6 and 9 hour. The annealed specimens were labeled as HEO-$T_{200}H_3$, HEO-$T_{200}H_6$, HEO-$T_{200}H_9$, HEO-$T_{400}H_6$, HEO-$T_{600}H_6$ and HEO-$T_{1000}H_6$, where the subscripts of T and H denoted the corresponding annealing temperatures and times. The non-annealed specimen was labeled as HEO-T_0H_0.

Electrochemical measurements

The electrocatalytic performances were measured on an electrochemical analyzer (CHI 660E) at 25°C. The electrochemical OER was happened in a typical three-electrode system, using specimen on the the nickel foam as the working electrode, a saturated Hg/HgO electrode as the reference electrodes, and a graphite rod as the counter electrode. To prepare the working electrode, 5 mg specimen was mixed into a solution containing 240 µL ethanol, 240 µL deionized water and 20 µL 5 wt% nafion to form a slurry, and then 5 µL slurry was dropped on a

nickel foam (surface area: 1 cm^2) and air dried naturally. The electrolyte was 1.0 M KOH. The linear sweep voltammetry (LSV) was tested with the scan rate of 10 mV s^{-1}. And the polarization curves were also obtained by 85 % ohmic potential drop (iR) correction. Electrochemical impedance spectroscopy (EIS) data for all specimens and controls in three-electrode configuration in 1 M KOH aqueous electrolyte. The data were collected for the electrodes under 0 V vs Hg/HgO.

Characterizations

Powder X-ray diffraction (XRD) was measured by Bruker D2 phaser diffractometer with Cu Kα radiation (λ = 1.541 Å, V = 30 KV and I = 10 mA) with a step of 0.2 °/s. Field-emission scanning electron microscopy (SEM, JEOL JEM-7100F) and high-resolution transmission electron microscopy (HRTEM, JEOL JEM-2100) were utilized to characterize the morphology of specimens. X-ray photoelectron spectroscopy (XPS) was measured by a Thermo Scientific Kα spectrometer with a monochromatic Al Kα source at 1486.6 eV, the binding energy was corrected based on the C 1s photoelectron peak at 284.6 eV. The energy dispersive X-ray spectroscopy (FEI QUANTA 400FEG) was measured.

Computational methods

Simulation details

The structural, energetic and electronic performances of all systems were estimated by DFT simulations in CASTEP code.[49] The cutoff kinetic energy of 750 eV and k-point of 7×7×1 were tested to be converged on account of the norm-conserving pseudopotentials[50] and Perdew-Burke-Ernzerh functional of generalized gradient approximation (GGA).[51] The convergence tolerances were set to 0.01 eV/Å, 1.0×10^{-6} eV per atom and 5.0×10^{-4} Å for force, energy and displacement, respectively. The empirical correction of Grimme's scheme D2 was adopted to describe the $van der Waals$ interactions between intermediates and substrates.[52] The GGA+U with spin polarization was also adopted to describe the localized d states,[53] where U = 4.2, 4.2, 4.2 and 3.0 eV was applied for Fe, Co, Ni and Zr elements.[54]

The electrochemical model of OER in alkaline media could be divided into the four one-electron reactions:

$$* + OH^- \rightarrow OH^* + e^- \tag{Equation 1}$$

$$OH^* + OH^- \rightarrow O^* + H_2O\ (l) + e^- \tag{Equation 2}$$

$$O^* + OH^- \rightarrow OOH^* + e^- \tag{Equation 3}$$

$$OOH^* + OH^- \rightarrow * + O_2(g) + H_2O(l) + e^- \tag{Equation 4}$$

The adsorption energies of OH, O and OOH groups on substrates were calculated by following:

$$\Delta E_{O^*} = E(sub/O) - E(sub) - [E(H_2O) - E(H_2)] \tag{Equation 5}$$

$$\Delta E_{OH^*} = E(sub/OH) - E(sub) - [E(H_2O) - E(H_2)/2] \tag{Equation 6}$$

$$\Delta E_{OOH^*} = E(sub/OOH) - E(sub) - [2 \times E(H_2O) - 3 \times E(H_2)/2] \tag{Equation 7}$$

where E(sub/H$_2$O), E(sub/OH), E(sub/O) and E(sub/OOH) denoted the total energies of H$_2$O, OH, O and OOH groups on substrate. E(sub), E(H$_2$O) and E(H$_2$) were the energies of bare substrate, water, and hydrogen gas, respectively.

The detailed Gibbs free energy changes of steps 1-4 could be calculated by:

$$\Delta G_1 = \Delta G_{OH^*} - eU \tag{Equation 8}$$

$$\Delta G_2 = \Delta G_{O^*} - \Delta G_{OH^*} - eU \tag{Equation 9}$$

$$\Delta G_3 = \Delta G_{OOH*} - \Delta G_{O*} - eU \qquad \text{(Equation 10)}$$

$$\Delta G_4 = 4.92 eV - \Delta G_{OOH*} - eU \qquad \text{(Equation 11)}$$

where the sum of ΔG_{1-4} was fixed to the negative of experimental Gibbs free energy of formation of two water molecules ($-2\,\Delta_{H_2O}^{exp} = 4.92$ eV). The Gibbs free energy of ($H^+ + e^-$) in solution was estimated as the half energy of H_2 molecule at standard condition.

The overpotential of OER was determined by following formulas:

$$\eta^{theory} = U_{OER} - 1.23 \qquad \text{(Equation 12)}$$

$$U_{OER} = Max(\Delta G_{OH*},\ \Delta G_{O*} - \Delta G_{OH*},\ \Delta G_{OOH*} - \Delta G_{O*},\ 4.92\ eV - \Delta G_{OOH*})/e \qquad \text{(Equation 13)}$$

The correlations between the free energy changes of each one-electron OER step (ΔG_1, ΔG_2, ΔG_3 and ΔG_4) and the atomic/electronic structures of Fe^{3+} active sites (ε_d, ε_p and D_d) were fitted as:

$$\Delta G_1 = -2.093\varepsilon_d - 3.631 = -6.288\varepsilon_p - 25.573 = -0.490 D_d + 14.376 \qquad \text{(Equation 14)}$$

$$\Delta G_2 = 0.322\varepsilon_d + 1.863 = 0.960\varepsilon_p + 5.205 = 0.074 D_d - 0.877 \qquad \text{(Equation 15)}$$

$$\Delta G_3 = 0.633\varepsilon_d + 2.610 = 1.848\varepsilon_p + 9.014 = 0.146 D_d - 2.776 \qquad \text{(Equation 16)}$$

$$\Delta G_4 = 1.138\varepsilon_d + 4.078 = 3.480\varepsilon_p + 16.271 = 0.270 D_d - 5.803 \qquad \text{(Equation 17)}$$

Structural models

The structural models of three HEO surfaces were built by adjusting the contents of Fe, Co, Ni and Zr ions based on the experimental data of HEO-T_0H_0, HEO-$T_{200}H_6$ and HEO-$T_{400}H_6$ specimens in Figure 3A, the contents of O^{2-} ions were estimated by neutralizing the TM ions. The HEO surfaces of HEO-1 plus HEO-O-1, HEO-2 plus HEO-O-2 and HEO-3 plus HEO-O-3 systems respectively represented the corresponding surface models of HEO-T_0H_0, HEO-$T_{200}H_6$ and HEO-$T_{400}H_6$ specimens (see Figures S10 and S11), where HEO-O-1, HEO-O-2 and HEO-O-3 systems denoted the O group covered HEO-1, HEO-2 and HEO-3 systems (HEO-O) in alkaline environment. The vacuum space of 20 Å was adopted for all systems to avoid the interaction between two neighboring images. Then, the OER intermediates of OH, O and OOH groups were adsorbed on the main active site of Fe3+ ion based on the experiment data. During the geometry optimization, the bottom three atomic layers were fixed and the other atoms were relaxed adequately.

OER processes

The four one-electron OER processes were considered based on the Equations 1, 2, 3, 4, 5, 6, and 7.[55,56] The reactive Gibbs free energy of each step on the main active site of Fe^{3+} ion were evaluated by[57,58]:

$$\Delta G = \Delta E + \Delta E_{ZPE} - T\Delta S - eU \qquad \text{(Equation 18)}$$

where *E*, *ZPE* and *S* were the calculated total energy, zero point energy and entropy of each system, respectively. The room temperature of *T* = 300 K was considered. *e* = 1 denoted the transferred charge during each one-electron reaction, *U* denoted the applied potential *versus* reversible hydrogen electrode.

The pre-designed formula of D_d and the occupied volume of d electrons (V_d) was following[48]:

$$D_d = \frac{CN \times n_d}{V_d} \qquad \text{(Equation 19)}$$

$$V_d = \sum_{i=1}^{CN} \left(r_{Fe}^i\right)^3 = \sum_{i=1}^{CN} \left(d_{Fe-O}^i - r_O\right)^3 \qquad \text{(Equation 20)}$$

where r_{Fe} and r_O denoted the ionic radius of Fe^{3+} and O^{2-} ions. $CN = 5$ denoted the coordination number of surface Fe^{3+} ions. The Fe-O bond lengths (d_{Fe-O}) were listed in S1, the $r_O = 1.280$ Å was considered,[59] $n_d = 6$ was the d electron number of elemental Fe atom.